Pergamon

Int. J. Heat Mass Transfer. Vol. 41, No. 3, pp. 583–600, 1998

Printed in Great Britain
0017–9310/98 $19.00+0.00

PII: S0017–9310(97)00123–3

Heat transfer and flow visualization experiments of swirling, multi-channel, and conventional impinging jets

L. HUANG and M. S. EL-GENK†

Institute for Space and Nuclear Power Studies/Chemical and Nuclear Engineering Department, University of New Mexico, Albuquerque, New Mexico

(*Received* 17 *September* 1996 *and in final form* 18 *April* 1997)

Abstract—Heat transfer and flow visualization experiments were conducted to investigate and compare the performance of swirling and multi-channel impinging jets with that of a conventional impinging jet (CIJ), having the same diameter at the same conditions. Swirling impinging jets (SIJs) employed a 25.4 mm long solid insert at the exit of housing tube to divert the air flow through four narrow channels along the surface of the insert, with the desired swirl angle (θ of 15, 30 and 45°). The multi-channel impinging jet (MCIJ) had same dimensions as SIJs, except that the narrow channels in the solid insert were vertical ($\theta = 0°$). The local and surface average Nusselt numbers of MCIJ were generally much higher than those of CIJ. SIJs demonstrated large increases in both Nusselt numbers and significant enhancement in radial uniformity of heat transfer compared to MCIJ and CIJ; best results were for $\theta = 15°$ and jet spacing of 50.8 mm. Flow visualization experiments using smoke flow, smoke wires and water jet techniques revealed the mechanisms contributing to the higher and enhanced radial uniformity of heat transfer by SIJs. The smoke flow technique provided images of flow field between jet exit and impinged surface, while smoke wires showed details of flow field at and close to impinged surface. The water jet flow, seeded with tiny air bubbles as tracers, revealed details of flow field and induced mixing on the impinged surface. © 1997 Elsevier Science Ltd.

INTRODUCTION

Numerous experimental investigations of circular conventional impinging jets (CIJs) [1–4] have shown that they enhance heat transfer, but produce non-uniform radial distributions of the local and surface average Nusselt numbers. In these bell-shaped radial distributions, Nusselt numbers peak at or near the stagnation point, then drop exponentially with radial distance from the stagnation point. For some industrial applications, however, such as electronic cooling and chemical vapor deposition (CVD), both high values and radial uniformity of heat and mass transfer are important.

In an attempt to improve the radial uniformity of heat transfer by an impinging air jet, Ward and Mahmood [5] have introduced the swirling impinging jet (SIJ) concept, in which tangential flow components are introduced into the main air flow to cause it to swirl, at the expense of weakening axial flow, particularly at stagnation point. The swirl generator of Ward and Mahmood consisted of a straight tube, which had four longitudinal narrow slots in the side wall for introducing the tangential air flow to generate the swirling effect in the main air stream. The measured radial distribution of local Nusselt number was slightly more uniform than for a conventional impinging jet, but its values were significantly lower, particularly in the vicinity of the stagnation point.

Agafonov [6] introduced a swirl in the jet main air flow using a specially designed twister, or a swirl generator. In his experiments, the flow field on the impinged surface was limited to a small radial distance from stagnation point, $r/d_j < 3$. The measured radial distribution of the local Nusselt number was shaped like a saddle and was symmetric about the stagnation point. Nusselt number at stagnation point was about 70% lower than that for CIJ and away from stagnation point ($r/d_j > 2$), its values were only slightly higher than those for CIJ. In general, the swirl generator designs of both Ward and Mahmood [5] and Agafonov [6] were only partially effective in improving the radial uniformity of heat transfer on the impinged surface.

Recently, El-Genk and Huang [7, 8] and Huang and El-Genk [9] proposed a swirl generator design with four narrow channels. The swirl angle between the jet axis and the tangent to the narrow channels, θ, was varied from zero to 45°. Preliminary test results demonstrated improvement in the radial uniformity and large increases in values of the local and surface average Nusselt numbers [7–9]. However, to better understand the heat transfer performance of this swirl generator, additional heat transfer and flow field visualization experiments are needed.

Very little work has been reported on flow field

† Author to whom correspondence should be addressed.

NOMENCLATURE

A	heat transfer area [m^2]
d_j	inner diameter of jet housing tube [m]
G	air mass flux [kg m^{-2} s^{-1}]
h	vertical jet spacing [m]
h	heat transfer coefficient
k	air thermal conductivity [W m^{-2} K^{-1}]
P	electric power to heated strips [W]
Nu	local Nusselt number, hd_j/k
Nu_0	Nusselt number at stagnation point
Nu_{max}	peak local Nusselt number
Nu_{av}	surface average Nusselt number, equation (1)
Nu_m	mean Nusselt number
r	radial distance from stagnation point [m]
Re	Reynolds number at jet exit, Gd_j/μ
T_j	air temperature at jet exit [K]
T_w	temperature of impinged surface [K]
T_{av}	surface average temperature [K], equation (2).

Greek symbols

μ	air viscosity [kg m^{-1} s^{-1}]
ρ	air density [kg m^{-3}].

visualization of either CIJs or SIJs. Behbahani *et al.* [10] have used smoke flow and smoke wires techniques to visualize the air flow field of a CIJ at low vertical jet spacing, $h/d_j < 2$, on a small surface, $r/d_j < 2.0$. The photographed images of the flow field at a very low Reynolds number showed two small vortices forming on the impinged surface at the same radial distance from stagnation point [10].

Shlien and Hussain [11] also used the smoke wires technique to visualize a free plane jet flow. A turbulent large-scale flow structure was observed from contortions of the turbulent/non-turbulent interface, which was made visible through the use of multiple views and orientations of smoke-wires in the non-turbulent entraining flow. Their photographs of the flow field showed clear images of the boundary flow. Salce and Simon [12] also visualized the swirl air flow inside a cylindrical cavity using the smoke wires technique. The images of the flow field, however, were not clear and did not show the whole flow field.

This paper reports the results of heat transfer and flow visualization experiments which were performed to investigate and compare the performance and flow fields of the swirling jet design of El-Genk and Huang [7, 8] with those of a CIJ having the same diameter (12.7 mm) at the same conditions. The performance of these jets was evaluated in terms of the measured increases in the values of the local and surface average Nusselt numbers and the uniformity of their radial distributions on the impinged surface. Heat transfer experiments investigated the effects of: (a) jet spacing, $h = 12.7$–76.2 mm; (b) swirl angle, $\theta = 0$, 15, 30 and 45°; (c) air Reynolds number, $Re = 3620$–$17\,600$; and (d) radial distances from stagnation point, $r = 0$–65 mm. Flow field visualization experiments employed three techniques: smoke flow, smoke wires and a water jet, seeded with tiny air bubbles as tracers. The conditions in the flow field visualization experiments were similar to those in heat transfer experiments, except for using unheated impinged surfaces.

HEAT TRANSFER EXPERIMENTS

The heat transfer experiment setup [4] consisted of a heated flat surface, a jet assembly, a jet support frame, two air flow meters and a computer-controlled data acquisition system (Fig. 1). The vertical spacing of the jet from the impinged surface was adjusted by moving the jet housing tube along its axis perpendicular to the heated surface. This surface was made of a 0.0508 mm thick and 26 mm wide 321A stainless-steel foil strips and measured 140 × 140 mm. The strips were laid flat onto a 25.4 mm thick Bakelite slab overlaid on top of a 25.4 mm thick Plexiglas plate for additional thermal insulation. They were heated using a high current/low voltage dc power and their surface temperatures were measured radially in two perpendicular directions using a total of 29 type-K thermocouples, 14 in each direction plus one at stagnation point. Radiation losses from the heated surface were negligible since the highest surface temperature in experiments was only 370 K. More details on experiment setup, placement of surface thermocouples, and experiment instrumentation were given in refs. [4] and [8].

Heat conduction losses through the Bakelite and Plexiglas substrates were estimated at 1.7%, and the estimated uncertainties in temperature measurements were ±0.25 K, ±2% in air volumetric flow rate, and ±0.7% in electric power supply. On the bases of the methodology outlined by Holman [13], the uncertainties in $Nu(r)$ and Re were ±4.5 and ±5%, respectively. The experimental results demonstrated good reproducibility; the variations in the measured local surface temperatures and Nusselt number in two perpendicular directions at the same radial locations were small and within the experimental uncertainties.

For each jet spacing, electric power to stainless-steel strips and the jet air volumetric flow rate were varied incrementally. After reaching steady state, the electric power input, air flow rate, surface temperatures, T_w,

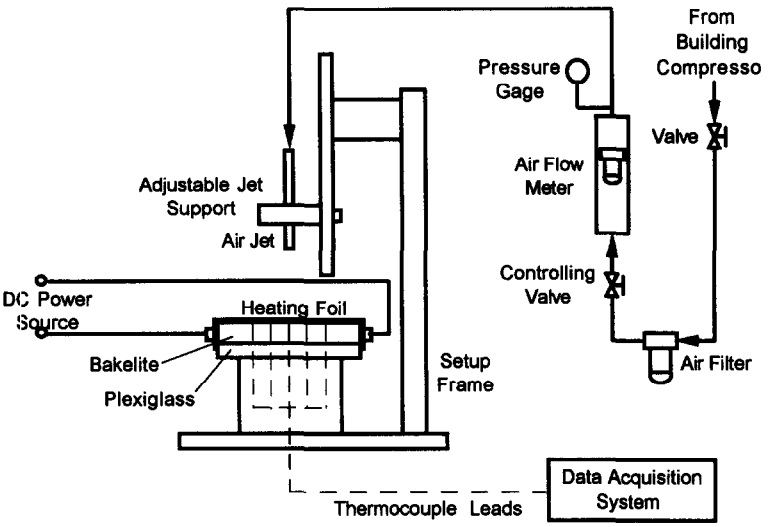

Fig. 1. A schematic of heat experiments setup.

and air temperature at jet exit, T_j, were recorded. Thermophysical properties of air in Nusselt numbers were evaluated at the average film temperature, $(T_w+T_j)/2$, while those in Re were evaluated at T_j. Although ambient temperature was not controlled in the experiments, the difference between air temperature at jet exit and ambient was small ~ 1.0 K.

Swirling jet assembly

The swirling jet assembly consisted of a housing tube (160 mm long) and a solid swirl generator insert which had four narrow flow slots machined on its surface (Fig. 2). The swirl angle was varied to change the direction and strength of the swirl in the air flow exiting the housing tube. When $\theta = 0°$, flow slots were vertical and the jet is referred to as multi-channel impinging jet (MCIJ). When $90° > \theta > 0°$, the jet is referred to as swirling impinging jet (SIJ). A conventional impinging jet (CIJ) had no inserts inside the housing tube. The lower end of the inserts for SIJs was displaced inward 12.7 mm from the housing tube exit to help the development of the swirling effect in the air flow (Fig. 2b). For the MCIJ, the lower end of the insert was installed flush with the lower end of the housing tube (Fig. 2d). The narrow slots machined onto the surface of the swirl generator insert were designed to increase turbulence intensity and alter the flow field on the impinged surface in order to enhance and improve the radial uniformity of heat transfer through the following effects [7, 8].

(a) increase the air mass flux in the perimeter region of the jet flow field in order to enhance turbulence in the portion of impinged surface away from stagnation point. The introduced swirls caused the flow envelop to spread radially outward via entrainment of surrounding air, hence increasing the radius of the affected area on impinged surface.

(b) block the air flow in the central region of the housing tube in an attempt to lower the heat transfer coefficient at and near stagnation point, thus improving the radial uniformity of heat transfer on the impinged surface.

The choice of structure material for the jet housing tube and the swirl generator depends on the application, whether it is cooling or heating. For the former, low temperature materials such as Plexiglas may be used. In heating applications, however, high temperature materials such as metals or ceramics may be considered depending on air temperature. The present jet housing tube was Plexiglas (wall thickness = 3.25 mm and $d_j = 12.7$ mm) and the swirl generator insert was made of a 25.4 mm long Plexiglas rod having a diameter equal to inner diameter of housing tube. Four narrow longitudinal slots were machined on the surface of the Plexiglas rod, 90° apart (Fig. 2a). Each slot had an approximately rectangular cross-section and an effective flow area of about 4.59 mm^2. The swirl generator insert was glued to the inner surface of housing tube. For a given air volumetric flow rate, the flow velocity in the narrow slots of the insert increased by the ratio of the flow area of the housing tube to the sum of areas of the four slots (area ratio of ~ 7.0).

FLOW VISUALIZATION EXPERIMENTS

Flow visualization experiments were performed using the same jet assembly as in heat transfer experiments, a strong light resource, a black background, and a camcorder and a 35 mm camera to record images of the flow fields. Three flow visualization techniques were used: smoke flow, smoke wires, and a water jet. The smoke flow technique was used to show the flow field between jet exit and impinged surface, while the smoke wires technique gave clear images of the flow field at and close to the impinged surface. When used together, the smoke flow and smoke wires gave images of the complete flow field, both between

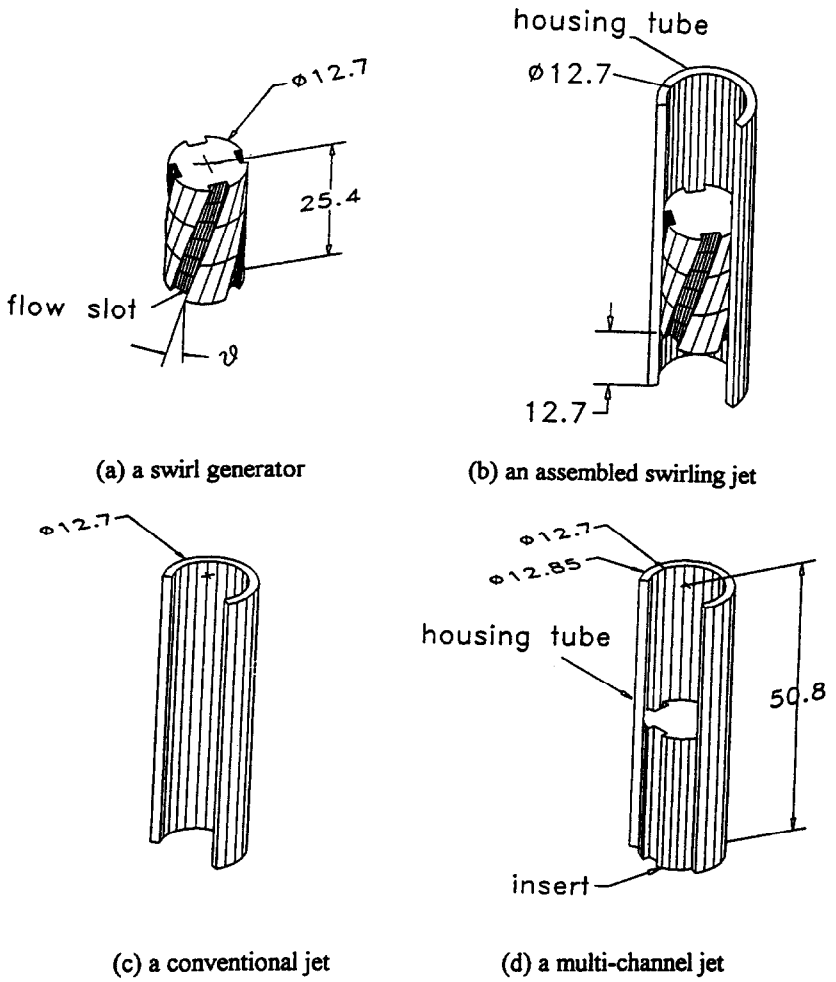

Fig. 2. Cross-sectional views of swirling and multi-channel impinging jet designs.

the jet exit and impinged surface, and horizontally along impinged surface, up to 65 mm from stagnation point. The water jet technique, however, showed how swirls affected the flow field and induced mixing on the impinged surface.

Smoke wires technique

Figure 3(a) shows a schematic of the smoke wires experiment setup. The nickel–chromium smoke wires, 0.25 mm in diameter and 270 mm long wrapped in fiberglass insulation, were spaced vertically 10 mm apart. Based on visual observations, the interruption to the air flow field by smoke wires was insignificant. Wires were held in place by attaching their ends to the walls of the Plexiglas support frame using tension springs, which kept them properly starched while being heated. The number of wires heated varied from one to seven, depending on jet spacing in the experiment. Electric power to smoke wires was adjusted to control the amount of smoke in the jet air flow field. The fiberglass insulation was moistened between experiments with a smoke oil composed of commercial-grade mineral oil and small amounts of anise oil and blue dye; it held enough oil to perform flow field visualization without interruption for a few minutes.

Smoke flow technique

In smoke flow visualization experiments, the air flow was mixed with smoke generated in a small chamber, Fig. 3(b), before entering the jet housing tube. The Plexiglas mixing chamber had 22 smoke wires, similar to those used in the previous technique. The outer diameter of smoke wires, including the fiberglass wrap, was about 1.5 mm. Electric power to heat wires and number of wires heated in the chamber depended on the amount of smoke needed and the value of the air flow rate in the experiment. When all wires were heated, they produced enough smoke for over 2 min of flow field visualization.

Water jet technique

The water jet flow visualization experiments were conducted to generate images of the flow field on the impinged surface, since water flow is easier to trace than air. The water jet housing tube was held in air above a horizontal, unheated Plexiglas surface, which was submerged in a Plexiglas water tank measuring

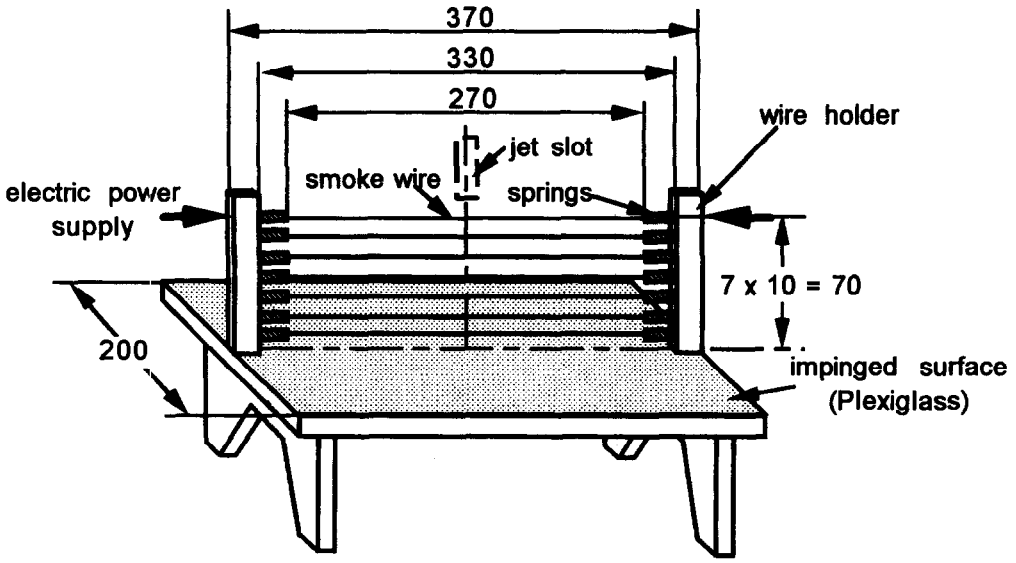

(a) Smoke Wires Setup

March

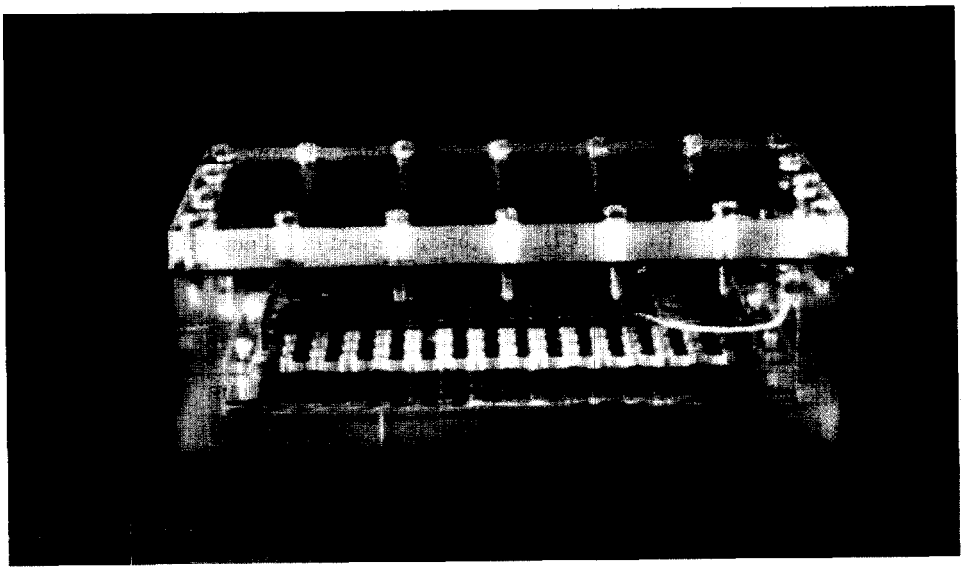

(b) Smoke Generator

Fig. 3. A schematic of smoke wires setup and a photograph of smoke generator.

$600 \times 600 \times 250$ mm. The water level above the impinged surface (116 mm) was kept constant during experiments. The tank was large enough to minimize the effect of confinement on the induced flow field. A mirror was mounted at 45° inclination below the impinged surface in the water tank to observe and record images of the flow field induced on the surface. To clearly visualize the induced flow filed on impinged surface, the water jet was seeded with tiny air bubbles as tracers.

HEAT TRANSFER RESULTS

The important features of El-Genk and Huang's [7, 8] swirl generator design are basically the dimensions and swirl angle of the narrow slots on its surface (Fig. 2). In order to determine the separate effect of each of these two features, the measured radial distributions of $Nu(r)$ for the MCIJ ($\theta = 0°$) were compared with those for a CIJ having the same diameter at the same conditions. Then, the experimental values of $Nu(r)$ for the MCIJ and a SIJ having a swirl angle of 15°, were compared to quantify the effect of the swirl angle on heat transfer.

Multi-channel jet heat transfer

Figure (4) shows that $Nu(r)$, for both the MCIJ and CIJ, decreased with increased radial distance from the stagnation point; however, values for the MCIJ were much higher than those for CIJ, particularly at and near the stagnation point. The effect of jet spacing, h on $Nu(r)$ was also much more significant for the MCIJ than CIJ, whereas $Nu(r)$ for both jets decreased as h increased. For example, at $Re = 8.8 \times 10^4$, Nusselt number at stagnation point, Nu_0, for CIJ decreased about 50% (from 1350 to 705) as h was increased from 12.7 mm to 76.2; compared to a decrease of only ~17% for CIJ. The value of Nu_0 for the MCIJ was 250 and 254% higher than that for CIJ at $h = 12.7$ and 76.2 mm, respectively.

While Nu_0 increased as h was decreased, $Nu(r)$ values away from stagnation point increased with increased h. For example, at $Re = 8.8 \times 10^4$ and $r = 60$ mm, $Nu(r)$ for MCIJ increased from ~200 to 246 (~23%) as h was increased from 12.7 to 76.2 mm. These results clearly demonstrated that MCIJ markedly enhanced heat transfer on impinged surface, compared to CIJ at the same Re. The pressure drop in MCIJ, however, was much higher than in CIJ (~1.26×10^4 Pa vs only ~25 Pa for CIJ at $Re = 1.76 \times 10^4$). Also, despite the significant enhancement in heat transfer, $Nu(r)$ for MCIJ was radially less uniform than for CIJ.

The pressure drop in SIJs was slightly higher than that in MCIJ and increased with increased swirl angle. For example, at $Re = 1.76 \times 10^4$, the pressure drop was estimated at 1.26×10^4 Pa, 1.29×10^4 Pa, and 1.24×10^4 Pa for θ of 15, 30 and 45°, respectively. These values, however, were about 24 times less when Re was decreased to 3620, at which results showed excellent radial uniformity of heat transfer on the impinged surface (Figs. 5 and 6).

Performance comparison of MCIJ and SIJ

Figures 5(a) and (b) compare the local Nusselt number radial distributions for MCIJ and a SIJ having $\theta = 15°$ at $Re = 88\,000$. Figure 5(a) shows that at a small vertical jet spacing, $h = 12.7$ mm, $Nu(r)$ values for MCIJ in the vicinity of stagnation point ($r \leqslant 0.5d_j$) were quite uniform, but decreased exponentially with increased radial distance. Conversely, the radial distribution of $Nu(r)$ for SIJ near stagnation point was non-uniform and had two peaks located about $0.5d_j$ on both sides of stagnation point; the peak $Nu(r)$ values were lower than those for the MCIJ. At a large radial distance from stagnation point ($r > 10$ mm), $Nu(r)$ for MCIJ was lower than that for SIJ. When jet spacing was increased to 76.2 mm, the values of $Nu(r)$ for SIJ were significantly lower, but radially more uniform than those for MCIJ [Fig. 5(b)]. Nusselt number values for both jets were lower at the large jet spacing, $h = 76.2$ mm [Fig. 5(b)].

Swirling jet heat transfer results

The following subsections present and discuss the results of heat transfer experiments of SIJs. These experiments investigated the effects of Re, h, θ and r on values and radial uniformity of both the local and surface average Nusselt numbers.

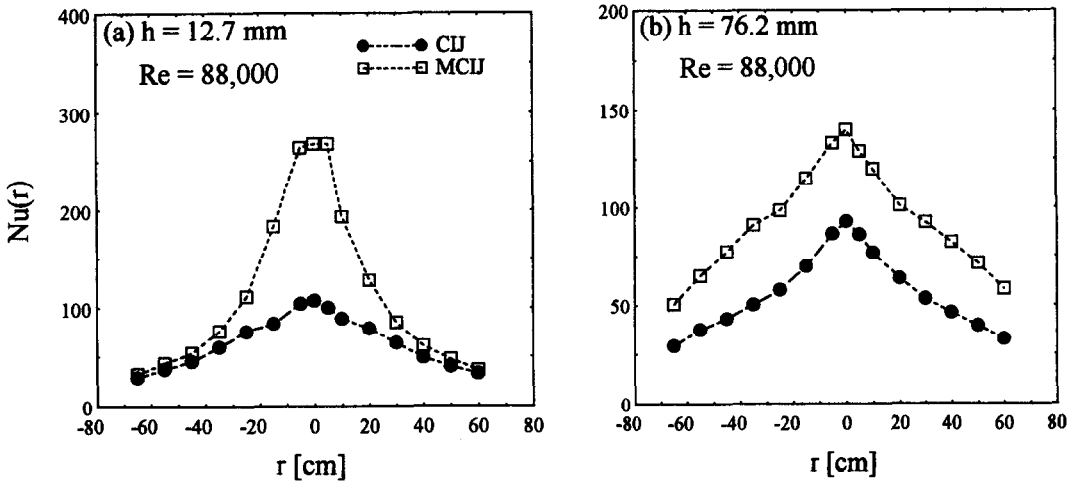

Fig. 4. Comparison of $Nu(r)$ values of MCIJ with those of CIJ.

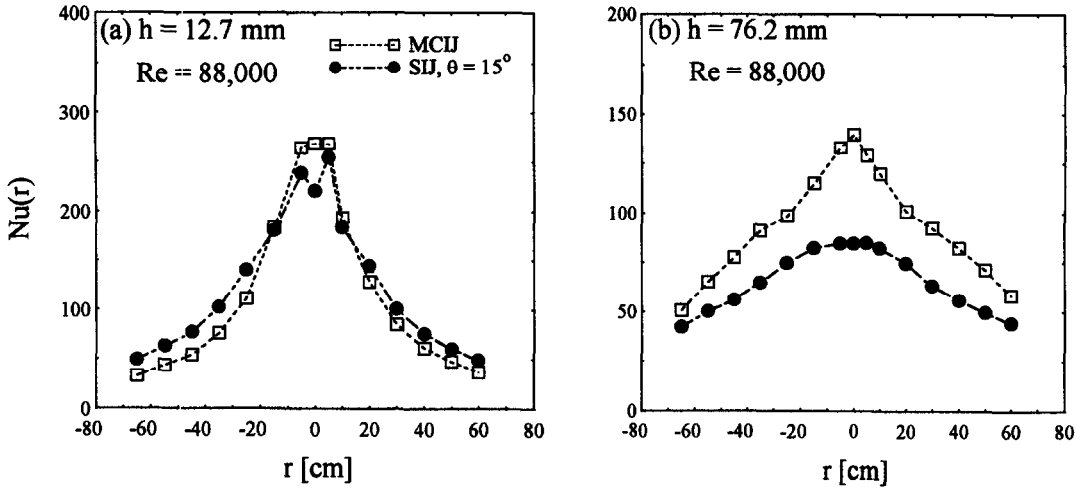

Fig. 5. Comparison of $Nu(r)$ values for a SIJ and the MCIJ at $Re = 88\,000$.

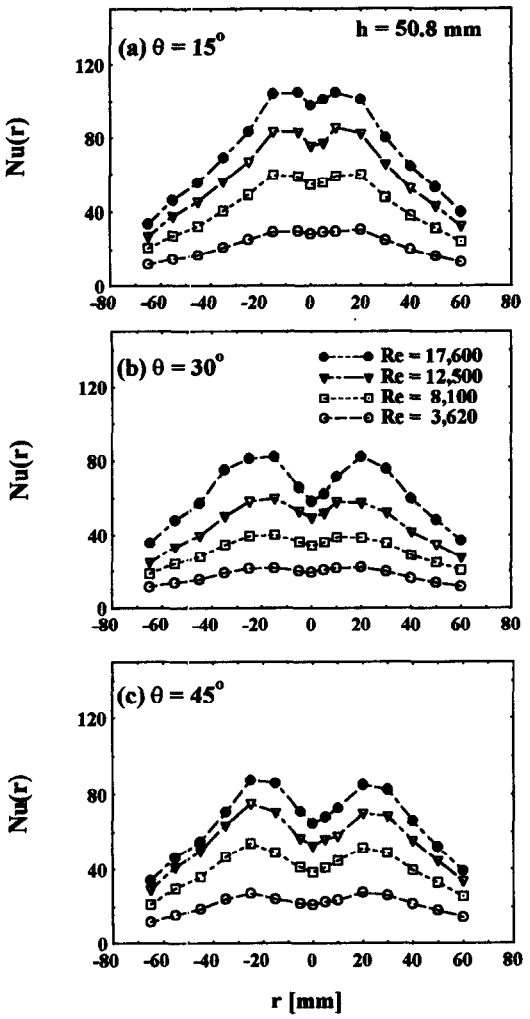

Fig. 6. Effect of swirl angle and Re on values of $Nu(r)$ for SIJs.

Effect of Reynolds number

Figure 6 shows measured $Nu(r)$ at different Reynolds numbers for SIJs with $\theta = 15$, 30 and 45°. At high Re, $Nu(r)$ had a saddle-shaped radial distribution, which was symmetric about the center line of the jet ($r = 0$), similar to that of Agafonov [6]. As swirl angle increased, the difference between peak Nusselt numbers and that at stagnation point increased. For the same θ, increasing Re increased $Nu(r)$ all along the heated surface, but only slightly affected the radial location of the peak Nusselt numbers. However, the difference between the peak Nusselt number and Nu_0 increased as Re increased, decreasing the radial uniformity of $Nu(r)$ in the vicinity of stagnation point, particularly for SIJs with $\theta = 30$ and 45°, Figs. 6(b) and (c).

Figure 6(a) also shows that for SIJ with $\theta = 15°$ at $h = 50.8$ mm and $Re = 8100$, $Nu(r)$ was uniform in an area having a radius $r \leqslant 20$ mm, which is about one and half jet diameter. For all Reynolds numbers investigated, highest and lowest $Nu(r)$ in this area were within 5% of their average values. The radial location of the peak values in the saddle-shaped radial distribution of $Nu(r)$ shifted outward as the swirl angle was increased, which affected the uniformity of heat transfer on impinged surface. For example, at $Re = 8100$, $Nu(r)$ for the SIJ with $\theta = 30°$ was almost uniform in an area having $r \leqslant 30$ mm, Fig. 6(b), but its values were much lower than those for $\theta = 15°$. Best results in terms of radial uniformity of $Nu(r)$ were achieved at Re of 3620, over an area having a radius $r < 20$ mm when $\theta = 15°$ and $r \leqslant 40$ mm when $\theta = 45°$.

Effect of swirl angle

Figure 7 quantifies the effects of swirl angle, Reynolds number, and jet spacing on the radial distributions of $Nu(r)$ for both SIJs and CIJ. At $r \leqslant 20$ mm, SIJ with $\theta = 15°$ gave higher $Nu(r)$ values than CIJ, Figs. 7(a) and (b), except for $h = 76.2$ mm and $Re = 8100$, Fig. 7(c). It is worth noting that SIJ with $\theta = 15°$ always produced a more uniform radial distribution of $Nu(r)$ than CIJ, Figs. 7(a)–(c). At the small jet spacing, $h = 12.7$ mm, $Nu(r)$ for all swirling

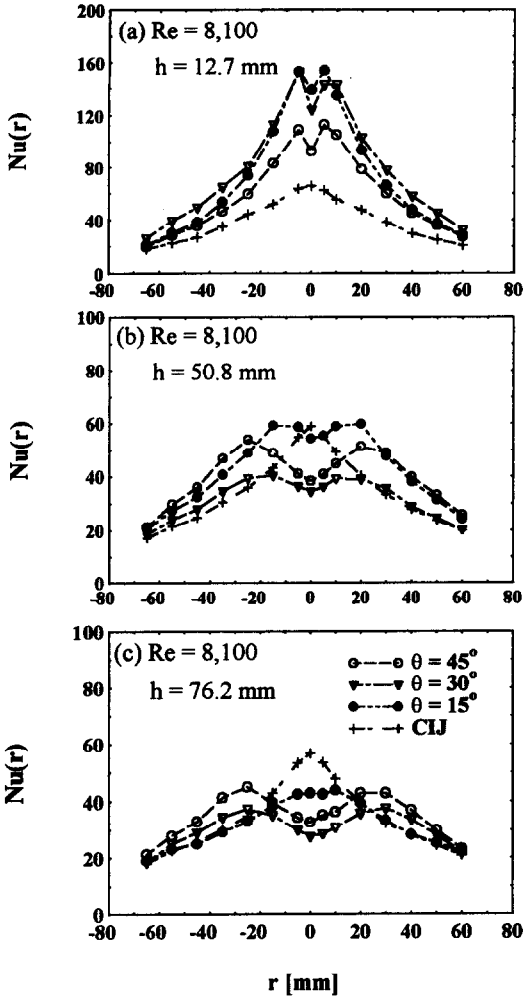

Fig. 7. Effect of jet spacing and Re on $Nu(r)$ values for SIJs.

jets investigated was higher than for CIJ, regardless of radial distance from stagnation point, Fig. 7(a). As h was increased to 50.8 mm, however, $Nu(r)$ for SIJs in the vicinity of stagnation point, $r \leqslant 20$ mm, was lower than for CIJ, Figs. 7(b) and (c). At the same jet spacing, but for $r \geqslant 20$ mm, $Nu(r)$ for SIJs with $\theta = 30$ and 45° SIJs was markedly higher than for CIJ. Thus, when $Nu(r)$ for SIJs was averaged over a large surface area, $r \geqslant 40$ mm, the surface average Nusselt number was also higher than for CIJ. At $h = 12.7$ mm, Fig. 7(a), SIJs with $\theta = 15$ and 30° gave higher and radially more uniform $Nu(r)$ values. At this jet spacing, SIJ with $\theta = 45°$ gave lower $Nu(r)$ values than those with $\theta = 15$ and 30°C.

At intermediate jet spacing, $h = 50.8$ mm, and $Re = 8100$, Fig. 7(b), $Nu(r)$ values for SIJ with $\theta = 45°$ for $r > 25$ mm were slightly higher than those for the other two SIJs. In Fig. 7(b), Nu_0, was about 20% lower than its peak value and this difference increased as Re increased. For $r > 20$ mm, $Nu(r)$ values for SIJ with $\theta = 15°$ were slightly lower than those for $\theta = 45°$, but for $r < 20$ mm, $Nu(r)$ for the former were significantly higher and radially more uniform than those for SIJs with $\theta = 30$ and 45°. For the SIJ with $\theta = 15°$, $Nu(r)$ in the vicinity of stagnation point, $r < 20$ mm, was radially uniform and close to its peak value. The radially most uniform $Nu(r)$ in the area with $r < 20$ mm was induced by SIJ with $\theta = 15°$ when $h = 50.8$ mm.

For $h = 50.8$ and 76.2 mm, Figs. 7(b) and (c), when a horizontal line representing $Nu_m = [(Nu_0 + Nu(r)_{max})/2]$ was drawn across, all values of $Nu(r)$ of SIJs with $\theta = 30$ and 45° for $r < 40$ mm were within 20% of their mean values, Nu_m, vs ~30–40% for CIJ. At large jet spacing, $h = 76.2$ mm, Fig. 7(c), however, $Nu(r)$ values for CIJ were higher than those for SIJs in the vicinity of stagnation point; but much lower than those of the SIJ with $\theta = 45°$, for $r > 25$ mm.

Effect of jet spacing

Figures 8(a)–(c) indicate that the dependence of $Nu(r)$ on swirl angle and jet spacing decreased with

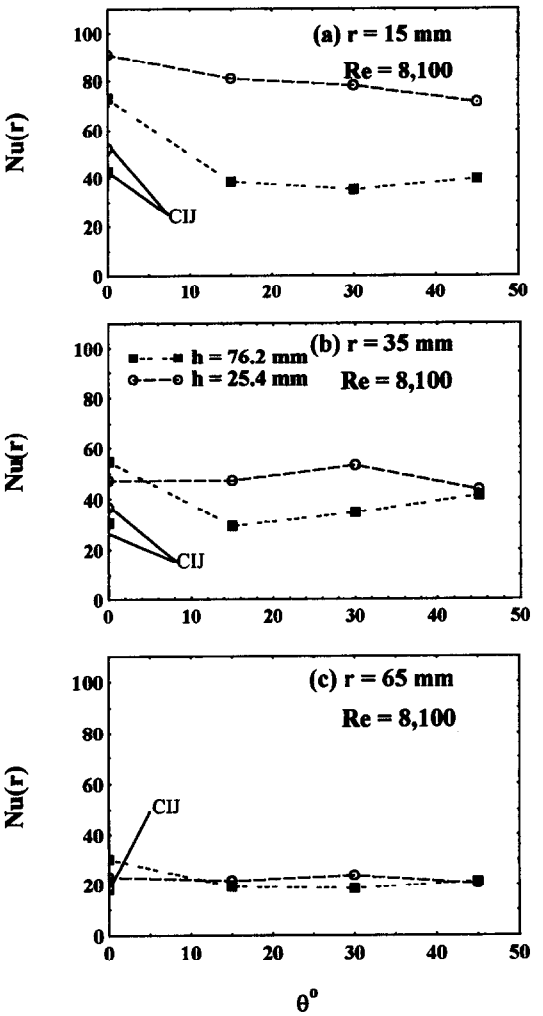

Fig. 8. Effect of swirl angle on $Nu(r)$ at different radial locations from stagnation point.

increased radial distance from stagnation point. At $r = 15$ mm and at an intermediate jet spacing, $h = 25.4$ mm, increasing swirl angle decreased $Nu(r)$ values. At a radial location further away from stagnation point, $r = 65$ mm, $Nu(r)$ value was almost the same as for CIJ and independent of swirl angle, Figs. 8(a) and (c). Figure 8 also shows that jet spacing had a more pronounced effect on $Nu(r)$ of SIJs at small than at large radial distances from stagnation point, Figs. 8(a) and (c).

Jet spacing had a significant effect on $Nu(r)$ of SIJs, particularly in the vicinity of stagnation point, Fig. 9. As jet spacing increased, $Nu(r)$ values decreased, but its radial uniformity improved. For example, at $Re = 8100$, peak $Nu(r)$ for the SIJ with $\theta = 15°$ decreased from 155 to 103 as h was increased from 12.7 to 25.4 mm; however, it decreased only from 58.6 to 42.8 when h was increased from 50.8 to 76.2 mm. At other Reynolds numbers, jet spacing had a similar effect on $Nu(r)$ of SIJs, except that higher Reynolds numbers induced higher, but radially less uniform $Nu(r)$ distributions (Fig. 10).

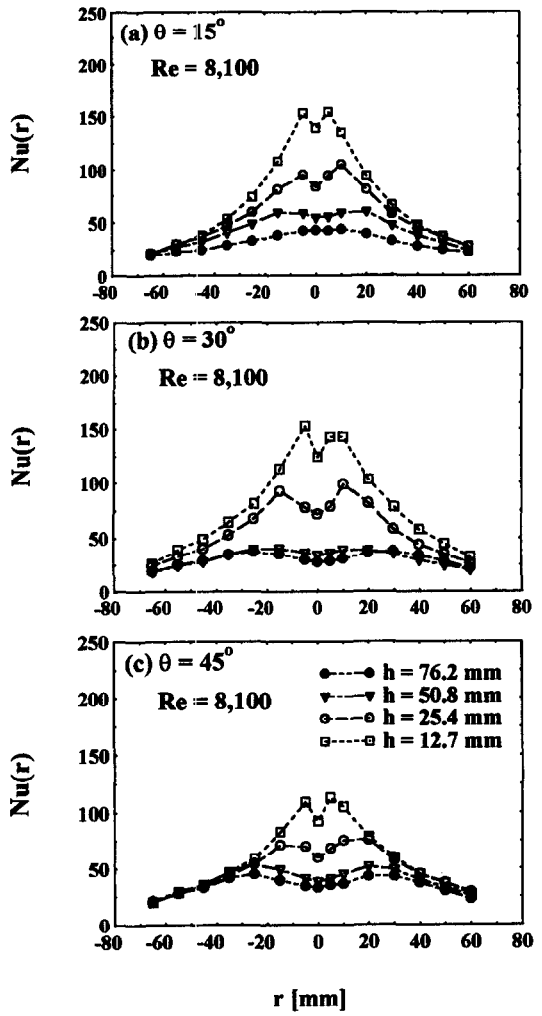

Fig. 9. Effect of jet spacing on $Nu(r)$ at different swirl angles and $Re = 8100$.

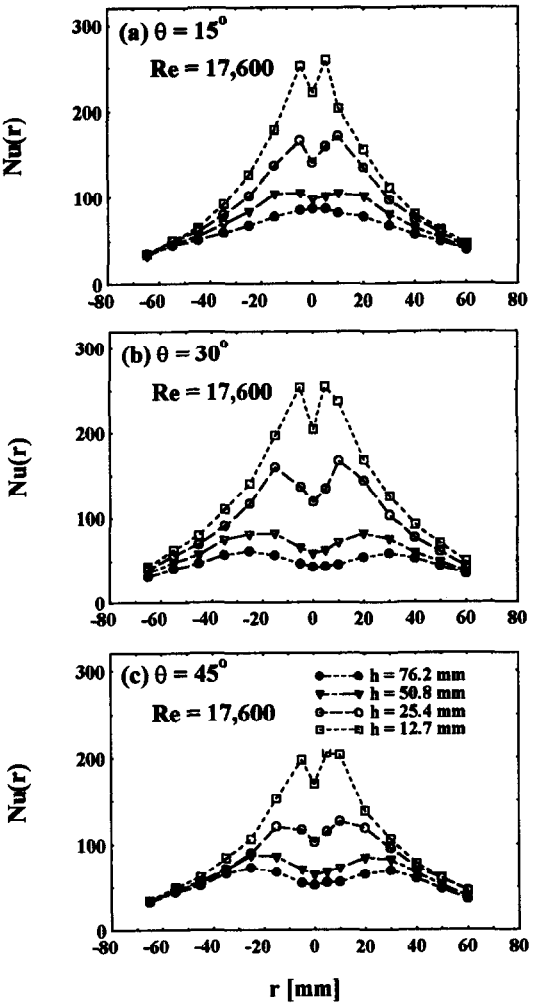

Fig. 10. Effect of jet spacing on $Nu(r)$ at different swirl angles and $Re = 17\,600$.

Uniformity of radial distribution of Nu(r)

To quantify the radial uniformity of heat transfer on impinged surface by SIJs, the ratios of $Nu(r)$ to its peak value, $Nu(r)_{max}$, were compared in Fig. 11. A high ratio indicates a smaller difference between the local and maximum Nusselt numbers, thus good radial uniformity of surface cooling. As delineated in Fig. 11, Nusselt number ratios for the CIJ were about 0.70, 0.50 and 0.38 at $r = 20$, 30 and 40 mm, respectively. These values were almost independent of jet spacing, but decreased with increased radial distance from the stagnation point, Fig. 11(a). For all SIJs investigated, however, increasing jet spacing increased Nusselt number ratio, indicating better radial uniformity of $Nu(r)$ (Fig. 11). For example, Nusselt number ratio for SIJ with $\theta = 30°$ at $r = 20$ mm increased from 0.8 at $h = 25.4$ mm to 0.95 at $h > 50$ mm. Another

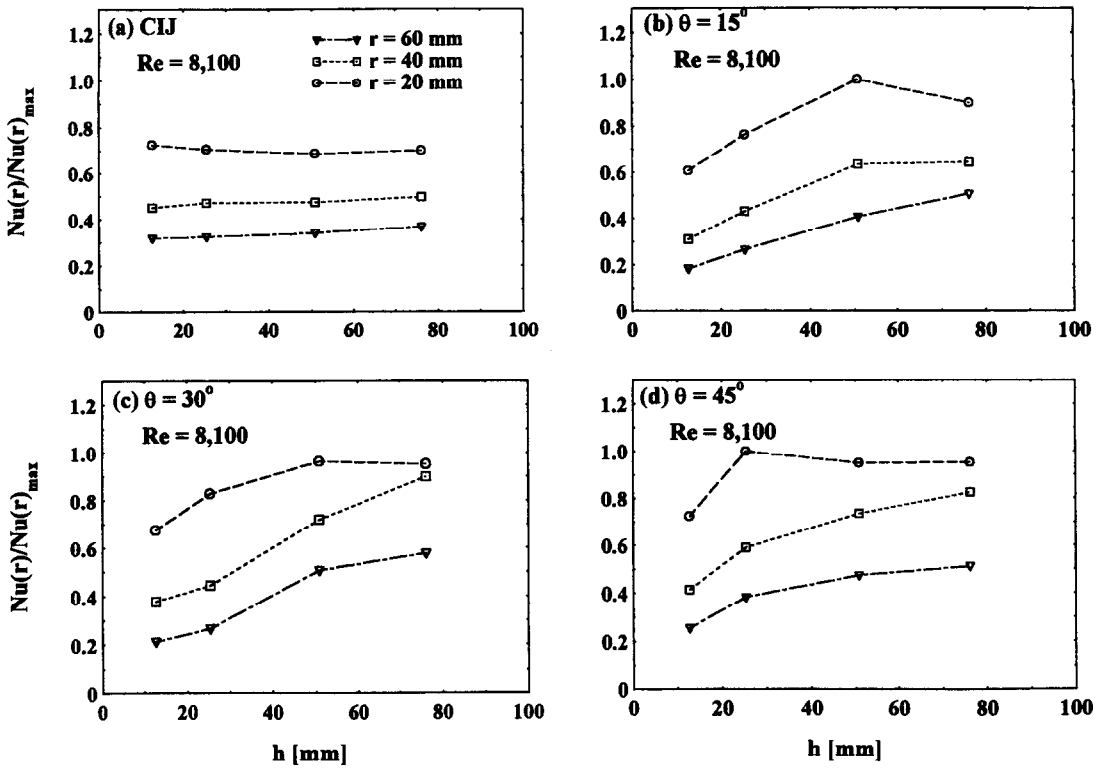

Fig. 11. Effect of jet spacing and swirl angle on radial uniformity of $Nu(r)$.

indicator of radial uniformity of heat transfer was the surface average Nusselt number, $Nu_{av}(r)$, whose values for SIJs are compared with those for CIJ in next subsections.

Surface average Nusselt number

The average Nusselt number in an area of impinged surface having a radius, r, was evaluated as follows:

$$Nu_{av}(r) = Pd_j/[Ak(T_w(r) - T_j)_{av}] \quad (1)$$

where $(T_w(r) - T_j)_{av}$ was calculated from the numerical integration of measured temperatures as

$$(T_w(r) - T_j)_{av} = \left(\frac{2}{r^2}\right)\int_0^r (T_w(r') - T_j)r'\,dr'. \quad (2)$$

Figure 12 shows that both swirl angle and jet spacing affected the values of $Nu_{av}(r)$ for SIJs and CIJ. For $h = 12.7$ and 25.4 mm, all SIJs gave much higher $Nu_{av}(r)$ values than CIJ. At $h = 25.4$ mm, SIJ with $\theta = 15°$ gave the best heat transfer performance, in terms of improved radial uniformity and higher $Nu_{av}(r)$ in the area with $r < 20$ mm. At high jet spacing, $h = 76.2$ mm, Fig. 12(c), $Nu_{av}(r)$ for SIJ with $\theta = 15°$ was almost uniform in the area with $r < 30$ mm, and its values were higher than those for the other two swirling jets. The SIJ with $\theta = 45°$ always gave higher $Nu_{av}(r)$ values over a large surface area, $r > 40$ mm, Fig. 12(c). Close to stagnation point, $r < 25$ mm, however, CIJ gave higher $Nu_{av}(r)$ values than SIJs. As Fig. 13 indicates, at low Reynolds number, $Re = 3620$, radial distributions of $Nu_{av}(r)$ for SIJs were almost flat. As Re increased, however, $Nu_{av}(r)$ became less uniform, exhibiting a saddle-shaped radial distribution. The radial location of peak $Nu_{av}(r)$ in the saddle-shaped radial distribution was almost independent of Re, but increased as the swirl angle increased; it was 22, 35 and 40 mm for $\theta = 15$, 30 and 45°, respectively.

The Nusselt number ratio $[Nu_{av}(r)/Nu(r)_{max}]$ was also used to quantify radial uniformity of heat transfer on impinged surface. Figure 14(a) reveals that at a small radial distance from stagnation point, $r = 24.2$ mm, $Nu_{av}(r)$ values were quite uniform whereas Nusselt number ratio was larger than 0.8 and almost independent on jet spacing. For $r = 40.2$ mm, Nusselt number ratio increased as jet spacing increased, Fig. 14(b). Jet spacing had a more pronounced effect on the Nusselt number ratio when $h \geqslant 50.8$ mm. The Nusselt number ratio for CIJ, however, was almost independent of jet spacing, but decreased with increased radial distance from stagnation point.

At low jet spacing, $h = 12.7$ mm, CIJ induced a relatively more uniform heat transfer than SIJs; however, Nusselt number values were much lower, Fig. 12(a). At $h = 25.4$ mm, SIJ with $\theta = 45°$ gave best radial uniformity of heat transfer, but values of $Nu_{av}(r)$ were lower than those for SIJs with $\theta = 15$ and 30°. As Fig. 14 indicates, in an area having a radius of one and a half jet diameters from stagnation point, when $h = 50.8$ mm, SIJ with $\theta = 15°$ produced excellent uniformity in heat transfer on the impinged

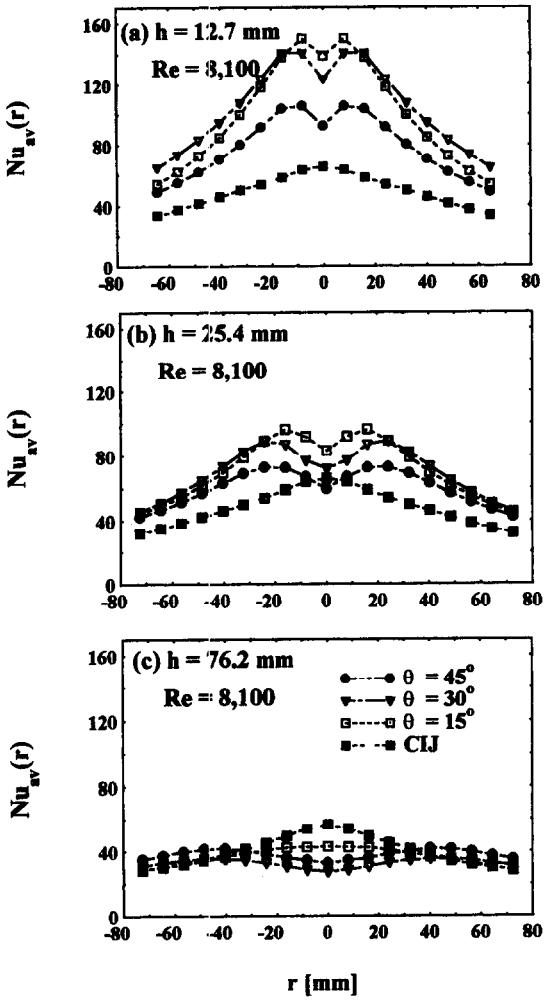

Fig. 12. Effect of jet spacing and swirl angle on $Nu_{av}(r)$.

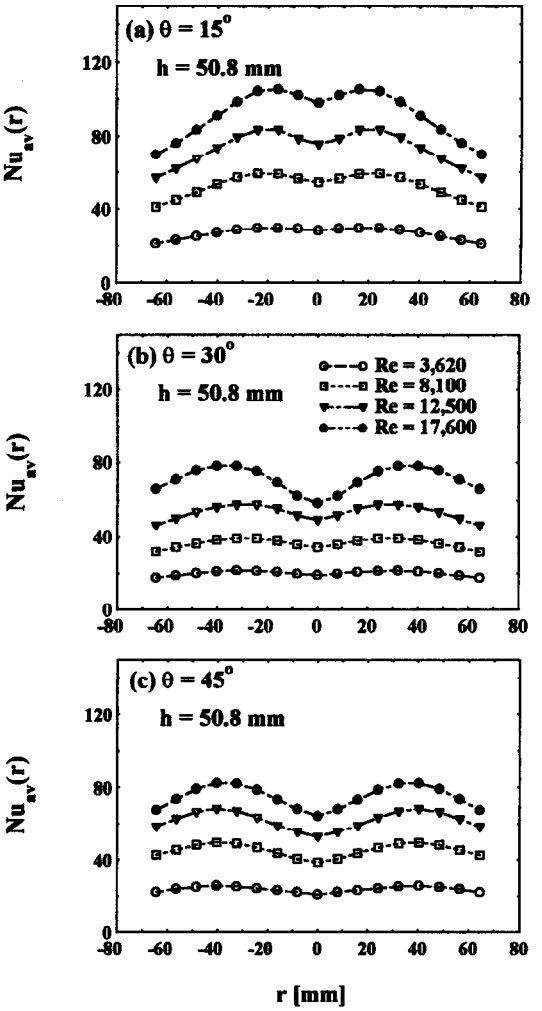

Fig. 13. Effect of Re and swirl angle on $Nu_{av}(r)$.

surface, whereas $[Nu_{av}(r)/Nu(r)_{max}] = 0.988$, and gave higher Nusselt numbers than all other jets. For a large heat transfer area having a radius >40 mm, SIJs with $\theta = 30$ and 45° gave the best radial uniformity in heat transfer on the impinged surface [Fig. 14(b, c)].

FLOW FIELD VISUALIZATION EXPERIMENTS RESULTS

The recorded images of the flow fields and induced mixing on the impinged surface by SIJs and MCIJ of El-Genk and Huang [8] and a CIJ having the same housing tube diameter at the same test conditions are presented and discussed.

CIJ flow visualization

Figure 15 shows photographs of the entire flow field induced by CIJ at $h = 76.2$ mm and $Re = 3620$–12 500, obtained by combining the smoke-jet and smoke-wires techniques. The flow field in the region extending from the exit of the jet tube to about one and half jet diameter from it was basically a parallel flow, which gradually changed to a narrow cone as it approached the impinged surface due to entrainment of surrounding air. The minor diameter of the CIJ flow cone was about one jet diameter, d_j, while its major diameter on impinged surface was $\sim 2d_j$. As a result, the intensity of flow turbulence by CIJ on impinged surface was highest at the centerline of jet (or at stagnation point), and grew gradually weaker with radial distance from stagnation point. The air flow impinging the surface developed into a parallel boundary layer along the surface, which subsequently formed vortices, some radial distance from stagnation point (Fig. 15). These vortices moved radially outward as either Reynolds number increased, Figs. 15(a)–(c), or jet spacing decreased, Figs. 15(b) and (d). The images of the flow fields of CIJ in Fig. 15 confirmed the measured radial distributions of $Nu(r)$ in heat transfer experiments, showing local Nusselt number peaking at or near stagnation point then decreasing exponentially with radial distance from the stagnation point.

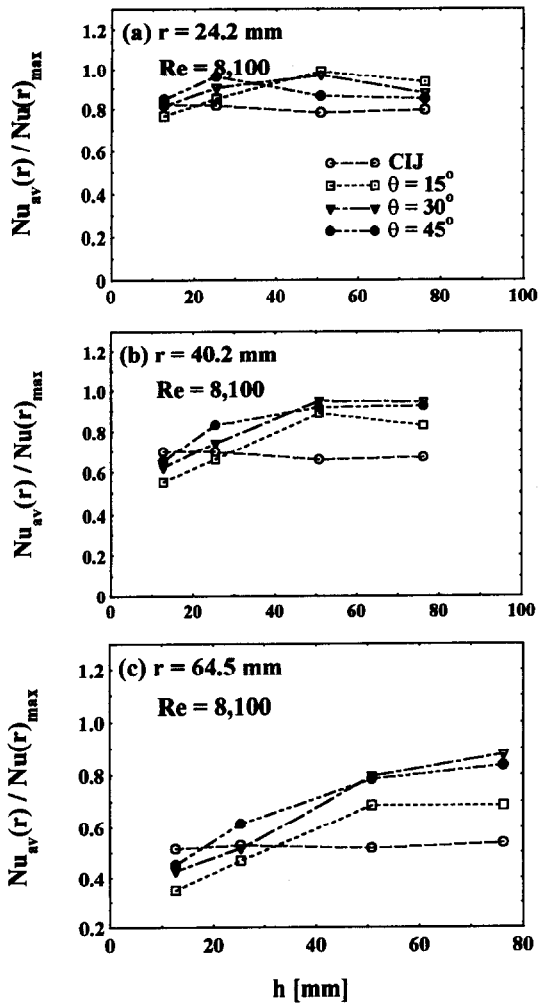

Fig. 14. Effect of jet spacing and swirl angle on radial uniformity of $Nu_{av}(r)$.

Flow fields of SIJs

Figure 16 compared the flow fields of CIJ, Fig. 16(a), MCIJ, Fig. 16(b), and SIJs with $\theta = 15°$, Fig. 16(c), and $\theta = 30°$, Fig. 16(d), at $Re = 8100$. The flow field of MCIJ showed four distinct parallel flow streams exiting the housing tube and continuing to about 1.5 jet diameter from jet exit before combining to form a flow cone similar to that of CIJ, but with a larger diameter at the top due to a higher entrainment of ambient air [Fig. 16(b)]. The spiral channels in the swirl generator insert of SIJs introduced angular flow components in the jet flow, causing it to spread radially outward shortly after exiting the housing tube. The radial spread of the flow of SIJs increased as swirl angle increased [Fig. 16(c, d)].

The narrow channels in the swirl generator introduced a twisting effect in the air flow exiting the housing tubes, Figs. 16(c) and (d). Figure 16(c) shows the twisted flow exiting the housing tube of SIJ with $\theta = 15°$ at $Re = 3620$. After about one jet diameter from the exit of housing tube, the four spiral air flow streams merged, forming a continuous flow cone [Fig. 16(c, d)]. The heat transfer on impinged surface was highest at the radial location where the jet flow cone impinged the surface. Outside and inside the flow cone, flow mixing, and hence heat transfer rate was lower, as discussed later.

When the swirl angle was increased to 30°, the jet flow field was shaped like a pyramid [Fig. 16(c)]. The spiral flow dominated in a vertical distance of about three jet diameters from the exit of housing tube. Below that, the flow spread widely in radial direction, impinging the surface over a larger distance from stagnation point than a SIJ with a smaller swirl angle [Fig. 16(c)]. The flow fields for SIJs explain the measured saddle-shaped radial distribution of $Nu(r)$ in heat transfer experiments, where the radial location of peak $Nu(r)$ corresponds to the radius of the jet flow cone on impinged surface (Fig. 17). The lower Nu_0 indicates that induced turbulence on the impinged surface inside the flow cone was weaker than at its surface. The induced turbulence outside the flow cone on impinged surface decreased with increased radial distance from the cone surface, confirming the heat transfer results (Fig. 6). These results showed $Nu(r)$ decreased exponentially with radial distance from the flow cone surface. Conversely, $Nu(r)$ inside the flow cone decreased with decreased radial distance from the cone surface, reaching a minimum at stagnation point.

The major radius of the SIJ flow cone at impinged surface increased as swirl angle increased (Fig. 17). This figure shows that SIJ with $\theta = 30°$ had a wider flow field, and hence, a larger impinged area than SIJ with $\theta = 15°$. The location of the peak $Nu(r)$ corresponds to the radial location where the flow cone impinged the surface [Fig. 17(c)].

Water jet flow field

Flow field visualization experiments conducted using non-submersed water SIJs produced images of the flow configuration and induced mixing on impinged surface (Fig. 18). Similar to air jets, the radial spread of the water jet on the impinged surface increased as swirl angle increased. Images of flow field inside the flow cone on impinged surface of a water SIJ with $\theta = 15°$ is shown in Fig. 11(a). This flow field was shaped like a donut where the most intense mixing occurred. Inside the donut, the flow fixing was relatively weaker, which explained by Nusselt numbers for SIJs at stagnation point were lower than that in the donut region, but higher than that for CIJ at the stagnation point (Fig. 6). The mean radius of the donut mixing region is equal to the radial location of peak value $Nu(r)$ (Fig. 6). Outside the donut mixing region of SIJ, spiral flow mixing also occurred, where the water flow spread radially outward in the form of four tangential streams to the perimeter of the donut region. Each flow stream belonged to one of the spiral channels in the swirl generator insert. The wide radial spread of this spiral flow mixing region caused the values of $Nu(r)$ in this region to be higher than those

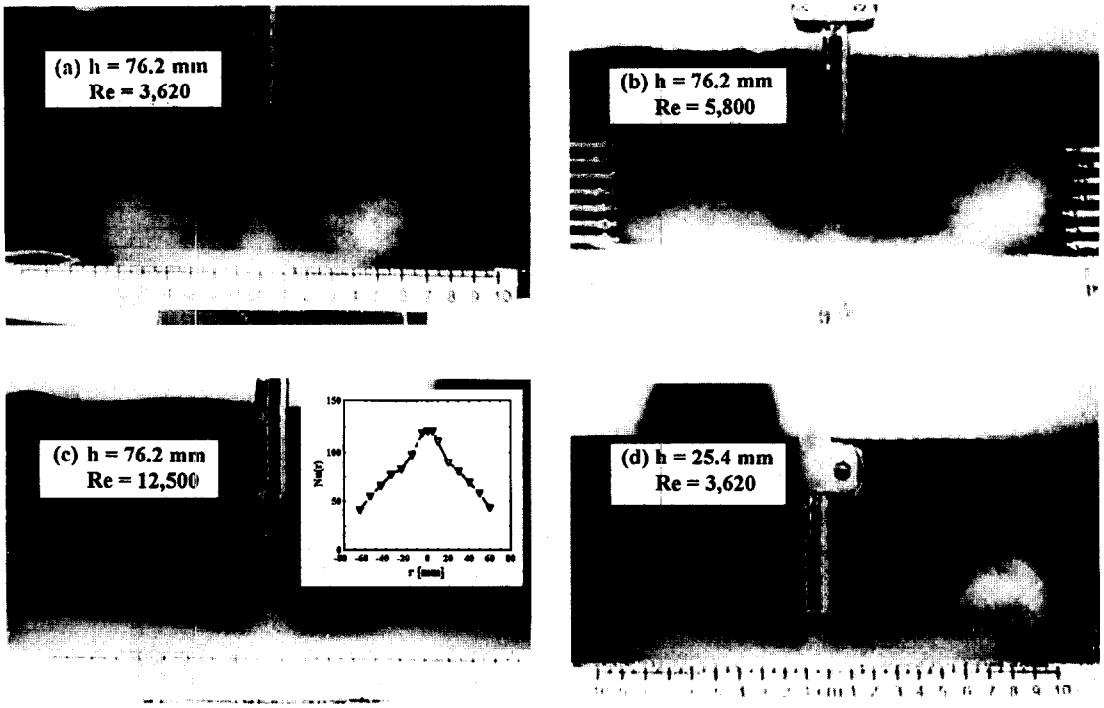

Fig. 15. Photographs of flow field of CIJ using smoke jet and smoke wires techniques.

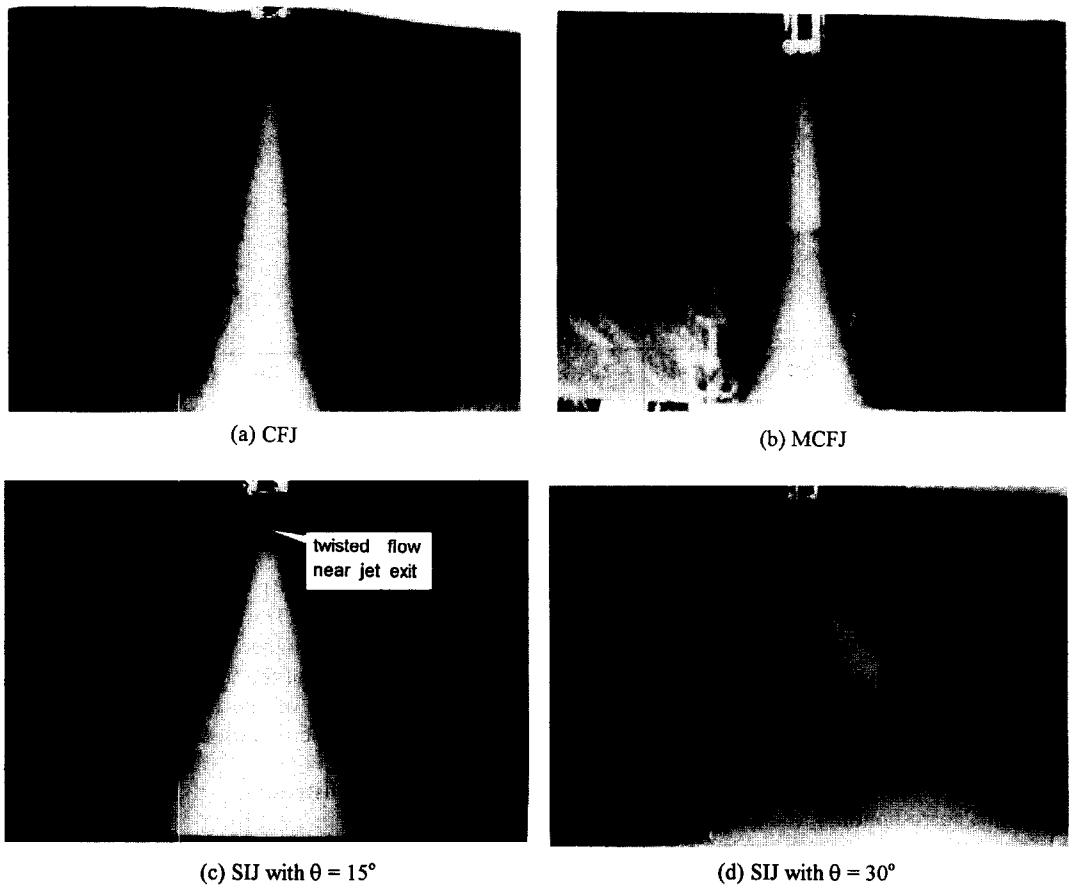

(a) CFJ (b) MCFJ

(c) SIJ with θ = 15° (d) SIJ with θ = 30°

Fig. 16. Comparison of flow fields of CIJ, MCIJ, and SIJs at $Re = 8$.

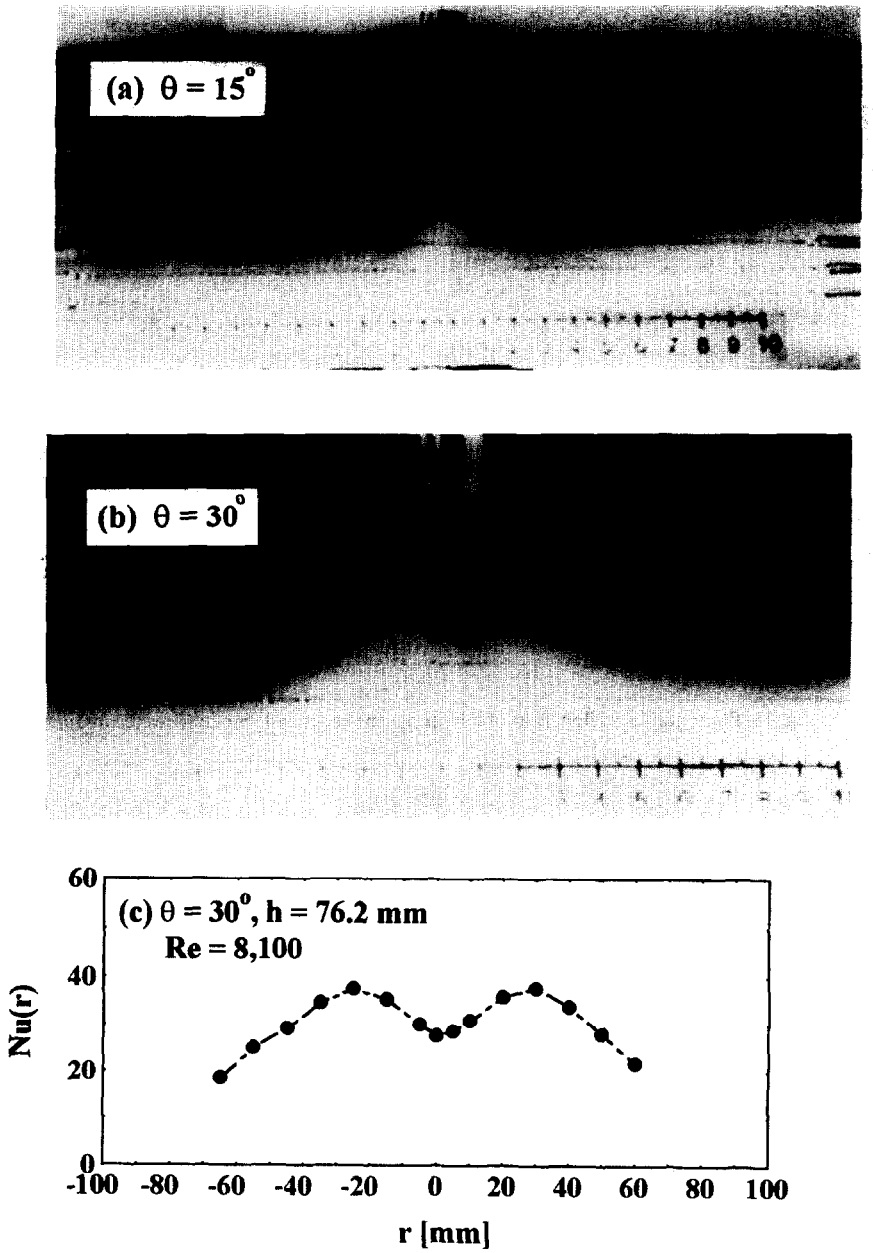

Fig. 17. Flow fields for SIJs and corresponding radial distribution of $Nu(r)$ for $q = 30°$.

for CIJ, but decreased rapidly with increased radial distance from the outer boundary of the donut mixing region. Clear images of the flow field on the impinged surface using a water jet were made possible by injecting tiny air bubbles as tracers in the water flow before entering the swirl insert.

After impinging the surface, the water flow for MCIJ, $\theta = 0°$, had developed into four strong radial components, corresponding to the four narrow channels of the MCIJ insert, which caused higher mixing in the vicinity of the stagnation point. These images of flow field explained the measured higher values of $Nu(r)$ for the MCIJ compared to those of CIJ at same conditions (Fig. 4). The mixing occurring at stagnation point by MCIJ was also more efficient than by CIJ, resulting in higher values of $Nu(r)$ for the former in the vicinity of the stagnation point (Fig. 4). Based on the results of the flow field visualization and heat transfer experiments, flow field models were developed for the CIJ and SIJs, Fig. 9, and discussed in the following subsections.

CIJ flow field

The flow field for a CIJ, extending from the exit of the jet housing tube to impinged surface can be divided into five characteristic regions: (1) free jet; (2)

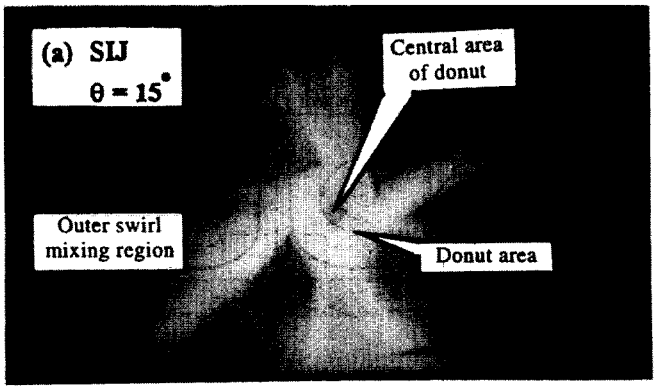

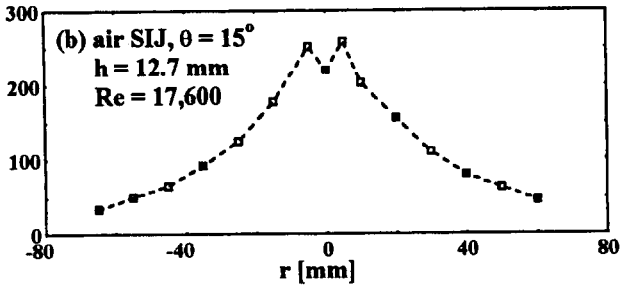

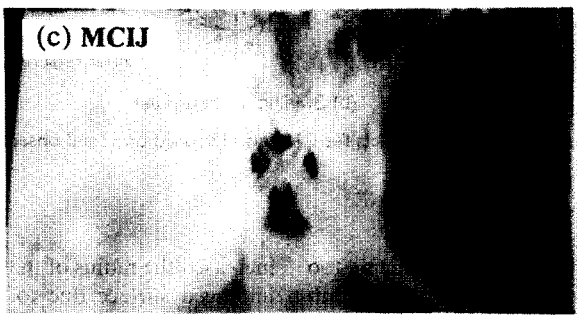

Fig. 18. Comparison of flow fields of MCIJ and SIJs using water jet technique.

impinged or stagnation area; (3) cross flow or boundary layer; (4) flow separation; and (5) entrainment [Fig. 19(a)]. Before impinging the surface, the air exiting the jet housing tube at a high speed of 20 ~ 140 m s^{-1} possesses the features of a free jet, Fig. 19(a), region 1. At $Re > 3260$, the exiting jet flow was turbulent, and would have become fully-developed after an axial distance $h/d_j > 20$ from jet tube exit. However, since in present experiments, as well as in most practical applications, h/d_j was much smaller than 20, the turbulent flow of CIJ was not fully developed as it impinged the heated surface.

Just below the free jet flow region, resided the impinged area region, Fig. 19(a), region 2. The impinged area by CIJ in the vicinity of the stagnation point was $\sim 1.5d_j$ high and had a radius of ~ 1–$1.5d_j$, depending on vertical jet spacing and Reynolds number. In this area, as the air jet impinged the surface part of the flow kinetic energy was converted into a static pressure, forcing the air to flow in a boundary layer along impinged surface, Fig. 19(a), region 3. Since the impinged surface area by CIJ was small compared to the entire heat transfer area influenced by the flow field, flow turbulence as well as $Nu(r)$ values outside this region decreased rapidly with increased radial distance from stagnation point. The air flow in the boundary layer (or cross flow region) decelerated quickly with increased radial distance from the stagnation point due to the increase in the flow cross-section area and the entrainment of surrounding air. As the boundary layer flow became laminar and thicker with increased radial distance from

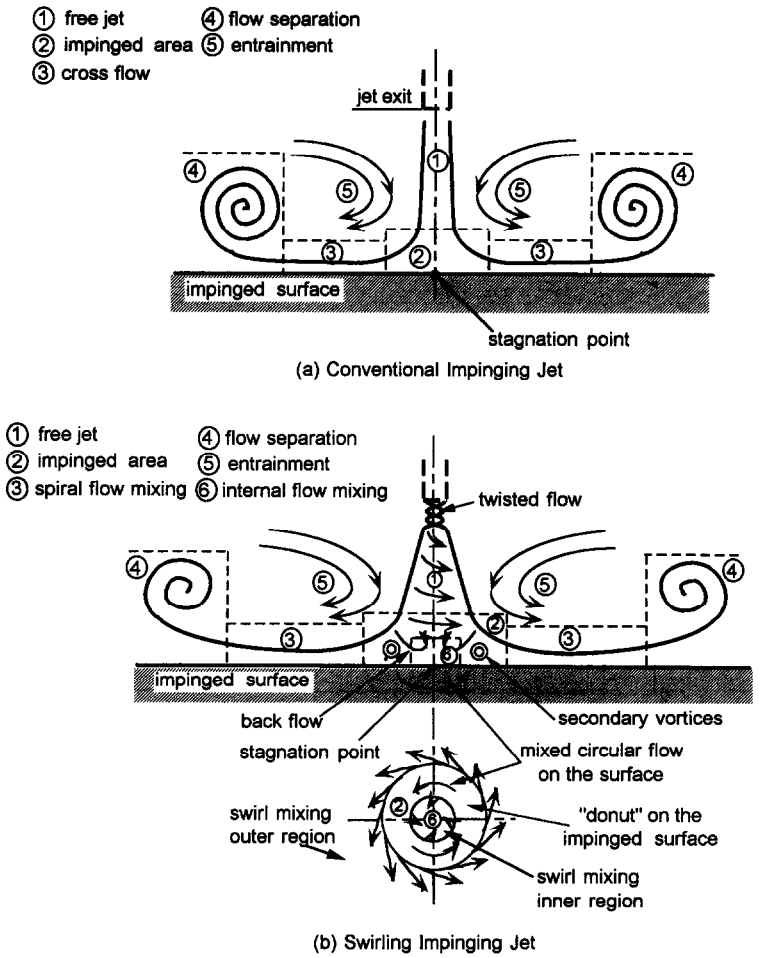

Fig. 19. Developed flow models for CIJ and SIJ based on visual observations.

stagnation point, the flow kinetic energy became too low to sustain radial flow. Subsequently, the combination effects of radial laminar flow and entrainment of surrounding air [Fig. 19(a), region 5] caused vortices to form at some distance from stagnation point, Figs. 15 and 19(a), region 4.

SIJ flow field

The flow field for the present SIJ design, Fig. 19(b), which was distinctly different from that of CIJ, Fig. 19(a), can be divided into the following regions: (1) free jet; (2) impinging area or donut flow mixing; (3) spiral flow mixing; (4) flow separation; (5) entrainment; and (6) internal flow mixing. The flow emerging from the four narrow channels in the swirl generator merged shortly after exiting the jet housing tube, forming a cone-shaped flow field (Fig. 16). The swirl caused the flow field to spread radially outward via entrainment of surrounding air, as it approached the impinged surface. The spiral effect and the high flow velocity of the air at the surface of the flow cone stimulated more entrainment of surrounding air than CIJ at the same conditions. Increasing either Re or h increased the radius of the flow cone at its base on the impinged surface due to additional entrainment of ambient air.

The impinged area of SIJ was significantly larger than that of a CIJ of the same diameter at the same conditions; $1–3d_j$ in diameter for the former vs $1–1.5d_j$ for the latter, depending on the values of swirl angle and vertical jet spacing, Fig. 19(b), region 2. The flow field of SIJ on the impinged area was shaped like a donut, Fig. 18. The intense flow mixing in the donut region caused the formation of the measured saddle-shaped radial distribution of $Nu(r)$, Fig. 6. The flow mixing in the central zone of the donut region was effective, but less intense than that in the donut region, resulting in a relatively higher heat transfer rate at the stagnation point than CIJ. The flow mixing, and, hence $Nu(r)$ in the inner zone of the donut region decreased with decreased radial distance from the inner surface of the donut. Conversely, the strength of flow mixing and values of $Nu(r)$ outside the donut region decreased with increased radial distance. The spiral flow outside the donut region spread the air flow field radially outward, along the impinged

surface, and the induced convection resulted in higher $Nu(r)$ values than for CIJ. Such enhancement in heat transfer outside the donut region was responsible for the improved radial uniformity of $Nu(r)$ by SIJs [6]. As either the swirl angle or jet spacing was increased, the average diameter of the donut region increased, causing the local Nusselt number peak value to move radially outward, resulting in a radially more uniform heat transfer. Regions 3 and 4 in Fig. 19 were basically the same as for CIJ, except that the radial location of the vortices was farther away from the stagnation point. Region 5 was also similar to that of CIJ, but much more pronounced due to higher entrainment of ambient air by SIJs.

SUMMARY AND CONCLUSION

Heat transfer and flow visualization experiments were performed to investigate and compare the heat transfer performance of new swirling jet designs with that of a conventional impinging jet having the same diameter at the same conditions. The performance of these jets ($d_j = 12.7$ mm) was evaluated in terms of the increases in the local and surface average Nusselt numbers and the improved radial uniformity of their radial distributions on the impinged surface. Heat transfer experiments investigated effects of: (a) jet spacing, $h = 12.7$–76.2 mm; (b) swirl angle, $\theta = 15$, 30 and 45°; (c) Reynolds number, $Re = 3620$–$17\,600$; and (d) radial distances from the stagnation point, $r = 0$–65 mm.

Flow field visualization experiments employed three flow visualization techniques: smoke flow, smoke wires, and water jet seeded with tiny air bubbles as tracers. The smoke flow technique showed the flow field between the exit of the jet housing tube and impinged surface, while the smoke wires technique gave clear images showing details of the flow field at and close to the impinged surface. When used together, the smoke flow and smoke wires techniques gave images of the complete image flow field, both between jet exit and impinged surface, and horizontally along impinged surface up to 65 mm from the stagnation point. The water jet technique showed clearly how swirl affected the flow field and mixing on the impinged surface. The three flow visualization techniques brought about a good understanding of the flow field including: air flow development after exiting the jet housing tube, flow mixing and formation of vortices on the impinged surface, and entrainment of ambient air.

Heat transfer experiments demonstrated that present SIJs induced markedly higher local and surface average Nusselt number values and improved the radial uniformity of heat transfer on the impinged surface compared to a CIJ having the same diameter at the same condition. SIJs produced saddle-shaped radial distributions of local and average Nusselt numbers, which were more pronounced at a high Reynolds number and/or small jet spacing. The double-peaks in the saddle-shaped radial distributions of $Nu(r)$ and $Nu_{av}(r)$ in the vicinity of stagnation point became less notable as Re decreased.

The radial uniformity of $Nu(r)$ and $Nu_{av}(r)$ of SIJs depended on values of the swirl angle, jet spacing, and air Reynolds number. In general, the radial uniformity of these Nusselt numbers improved as the swirl angle and/or jet spacing was increased. At $h = 50.8$ mm, the swirling jet with $\theta = 15°$ gave excellent results in terms of both higher values and improved radial uniformity of heat transfer in an area having a radius of one and half jet diameters from the stagnation point. For an area having a radius $r > 40$ mm, SIJs with $\theta = 30$ and 45° gave the best results in terms of the radial uniformity of heat transfers on the impinged surface.

Nusselt numbers for SIJs were higher than for CIJ at intermediate jet spacing, $h = 50.5$ mm. At higher jet spacing, $h = 76.2$ mm, however, Nusselt numbers for SIJs were generally lower than those for CIJ in the vicinity of the stagnation point, but higher at large radial distances from the stagnation point. Results also showed that $Nu(r)$ for MCIJ ($\theta = 0°$) at the stagnation point was about 250 and 154% higher than that for CIJ for $h = 12.7$ and 76.2 mm, respectively. At small jet spacing, $h = 12.7$ mm, MCIJ induced a radially more uniform distribution of $Nu(r)$ than CIJ in the vicinity of the stagnation point ($r < 9.0$ mm), regardless of the value of Re.

Acknowledgement—This research is sponsored by the University of New Mexico's Institute for Space and Nuclear Power Studies (ISNPS).

REFERENCES

1. Martin, H., Heat and mass transfer between impinging gas jets and solid surfaces. *Advances in Heat Transfer*, 1977, **13**, 1–60.
2. Goldstein, R. J. and Seol, W. S., Heat transfer to a row of impinging circular air jets including the effect of entrainment. *International Journal of Heat and Mass Transfer*, 1991, **34**, 2133–2147.
3. Jambunathan, K., Lai, E., Moss, M. A. and Button, B. L., A review of heat transfer data for single circular jet imp. *International Journal of Heat and Fluid Flow*, 1992, **13**, 106–115.
4. El-Genk, M. S. and Huang, L., Local and average Nusselt number correlations for an impinging air jet. *30th National Heat Transfer Conference*, Vol. HTD-303, 1995, pp. 34–41.
5. Ward, J. and Mahmood, M., Heat transfer from a turbulent, swirling, impinging jet. *7th International Heat Transfer Conference*, Vol. HTD-3, 1982, pp. 401–407.
6. Agafonov, K. N., Heat transfer in a turbulent twisted jet incident on a plane barrier. *Heat Transfer Soviet Research*, 1991, **23**, 378–383.
7. El-Genk, M. S. and Huang, L., Compact impinging jet for enhanced heat transfer. IMechE Conference Transaction-1995-2, Paper no. C510/036/95. *4th U.K. Heat Transfer Conference*, Manchester, U.K., 1995.
8. El-Genk, M. S. and Huang, L., Apparatus for enhancing mass transport and heat transfer. Patent (pending), University of New Mexico, Albuquerque, New Mexico, 1996.

9. Huang, L. and El-Genk, M. S., Heat transfer and flow visualization of swirling impinging jets. *31st National Heat Transfer Conference*, Vol. HTD-324, 1996, pp. 93–100.
10. Behbahani, A. I., Disimile, P. J. and Aydore, S., Flow visualization in an impinging circular air jet. *24th National Heat Transfer Conference*, Portland, Vol. HTD-112, 1989, pp. 143–148.
11. Shlien, D. J. and Hussain, A. K. M. F., Visualization of the large-scale motion of a plane jet, flow visualization. *Proceedings of the 3rd International Symposium of Flow Visualization*, 1983.
12. Salce, A. and Simon, T. W., Investigation of the effects of flow swirl on heat transfer inside a cylindrical cavity. *Journal of Heat Transfer*, 1991, **113**, 5.
13. Holman, J. P., *Experimental Methods for Engineers*. McGraw-Hill, New York, 1984.